A Prototype Wearable Device for Noninvasive Monitoring of Transcutaneous Oxygen

Vladimir Vakhter¹⁰, Graduate Student Member, IEEE, Burak Kahraman¹⁰, Graduate Student Member, IEEE, Guixue Bu¹⁰, Foroohar Foroozan¹⁰, Senior Member, IEEE, and Ulkuhan Guler¹⁰, Senior Member, IEEE

Abstract—Transcutaneous oxygen monitoring is a noninvasive method for measuring the partial pressure of oxygen diffusing through the skin, which strongly correlates with changes in dissolved oxygen in the arteries. Luminescent oxygen sensing is one of the techniques for assessing transcutaneous oxygen. Intensity- and lifetime-based measurements are two well-known methods used in this technique. The latter is more immune to optical path changes and reflections, making the measurements less vulnerable to motion artifacts and skin color changes. Although the lifetime-based method is promising, the acquisition of high-resolution lifetime data is crucial for accurate transcutaneous oxygen measurements from the human body when skin is not heated. We have built a compact prototype along with its custom firmware for the lifetime estimation of transcutaneous oxygen with a provision of a wearable device. Furthermore, we performed a small experiment study on three healthy human volunteers to prove the concept of measuring oxygen diffusing from the skin without heating. Lastly, the prototype successfully detected changes in lifetime values driven by the changes in transcutaneous oxygen partial pressure due to pressure-induced arterial occlusion and hypoxic gas delivery. The prototype resolved a minimum change of 1.34 ns in a lifetime that corresponds to 0.031 mmHg in response to slow changes in the oxygen pressure in the volunteer's body caused by hypoxic gas delivery. The prototype is believed to be the first in the literature to successfully conduct measurements in human subjects using the lifetime-based technique.

Index Terms—Wearable, respiration monitoring, vital signs, physiological monitoring, PtcO₂, SpO₂, partial pressure of oxygen, transcutaneous oxygen, luminescent oxygen sensing, lifetime, hypoxia.

Manuscript received 28 October 2022; revised 20 December 2022 and 21 January 2023; accepted 12 February 2023. Date of publication 2 March 2023; date of current version 19 May 2023. This work was supported in part by the National Science Foundation (NSF) under Grant OAC-2203827, and in part by Analog Devices Inc. through a Research Gift. This paper was recommended by Associate Editor Hanjun Jiang. (Vladimir Vakhter and Burak Kahraman contributed equally to this work.) (Corresponding author: Ulkuhan Guler.)

This work involved human subjects or animals in its research. Approval of all ethical and experimental procedures and protocols was granted by the Institutional Review Board of Worcester Polytechnic Institute (FWA #00030698 - HHS #00007374) under Application No. IRB-22-0682, and performed in line with the the Code of Federal Regulations (45 CFR 46).

Vladimir Vakhter, Burak Kahraman, and Ulkuhan Guler are with the Electrical and Computer Engineering Department, Worcester Polytechnic Institute, Worcester, MA 01609 USA (e-mail: vvvakhter@wpi.edu; bkahraman@wpi.edu; uguler@wpi.edu).

Guixue Bu and Foroohar Foroozan are with the Analog Devices, Inc., Wilmington, MA 01887 USA (e-mail: guixue.bu@analog.com; foroohar.foroozan@analog.com).

Color versions of one or more figures in this article are available at https://doi.org/10.1109/TBCAS.2023.3251321.

Digital Object Identifier 10.1109/TBCAS.2023.3251321

I. INTRODUCTION

HE growing demand for remote health monitoring and therapy has led to the proliferation of miniaturized smart and connected health devices [1], [2], [3], [4], [5], [6]. As illustrated in Fig. 1, these emerging devices can produce real-time data on patient vital signs for clinical decision-makers to inform their treatment plans. Therefore, these devices are central to the development of cost-effective, patient-centered healthcare models that are more accessible, flexible, and proactive.

While medical wearable technologies have undergone a significant transformation, there are limitations in both the variety and the quality of the vital signs they provide. For instance, amid this transformation, there has been little progress in the miniaturization of respiration-sensing devices to a compact form factor [7], [8]. Yet, respiration issue is known as one of the early indicators of the onset of a patient's decline [9]. For example, the respiratory coronavirus disease 2019 (COVID-19) was the largest contributor (after heart disease and cancer) to the annual mortality burden in 2020 in the United States [10], [11]. A suitable environment for continuous and remote monitoring of respiratory parameters supported by wearable devices could allow for early detection of symptoms and timely medical interventions, reducing mortality [12].

The functions of respiration include ventilation (removing carbon dioxide, CO₂, from cells and tissues) and oxygenation (delivering oxygen, O₂, to cells and tissues). Evaluation of the respiratory efficiency and oxygenation of blood and tissues is a complex process that requires a comprehensive analysis of multiple parameters as a whole. In current clinical practice, oxygenation is assessed using three primary parameters:

- the arterial partial pressure of oxygen (PaO₂), reflecting the amount of unbound free oxygen molecules dissolved in plasma;
- the saturation of arterial oxygen (SaO₂), which is the ratio of oxygenated hemoglobin to the total hemoglobin; and
- the content of arterial oxygen (CaO₂), which is the total amount of oxygen molecules.

A noninvasive and widely accepted surrogate measure of oxygenation is presented by pulse oximetry, which assesses the peripheral blood oxygen saturation (SpO₂) to estimate SaO₂. The ease of use of pulse oximeters has made these devices ubiquitous; therefore, SpO₂ is widely used to track oxygen trends. Moreover, in some cases, SpO₂ is also used as an indirect method for estimating PaO₂. However, the relationship

1932-4545 © 2023 IEEE. Personal use is permitted, but republication/redistribution requires IEEE permission. See https://www.ieee.org/publications/rights/index.html for more information.

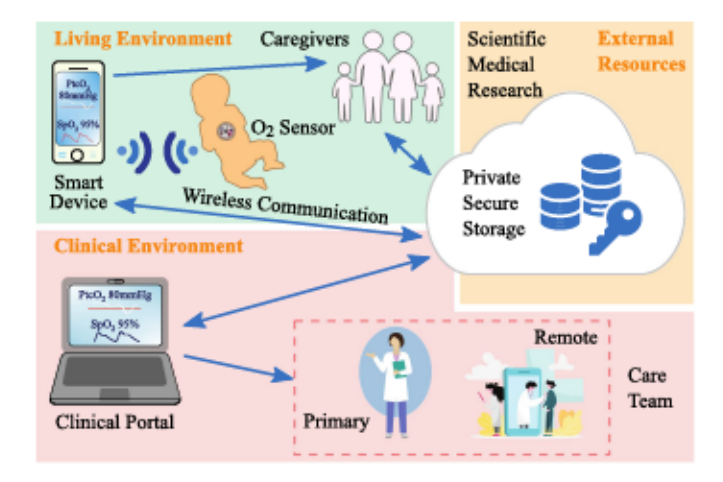


Fig. 1. Remote patient monitoring concept with smart wearable devices.

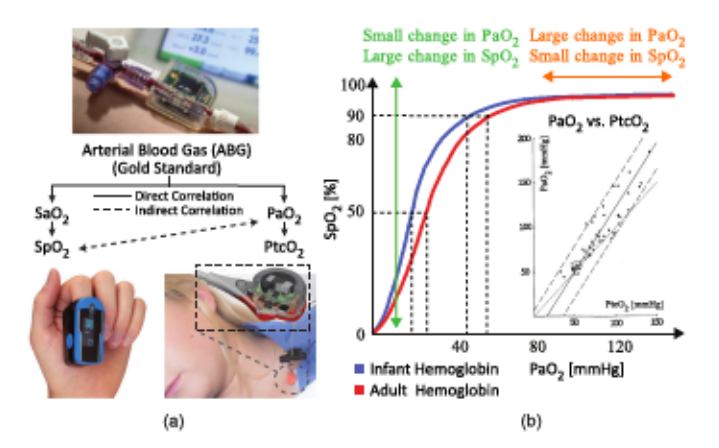


Fig. 2. (a) Oxygenation measurement methods and (b) the relation of oxygenation parameters shown on an oxy-hemoglobin dissociation curve [15] (SpO₂ vs. PaO₂) and an inset graph [16] (PaO₂ vs. PtoO₂). Adapted from [17].

between SpO₂ and PaO₂ is a sigmoid function, described by the oxy-hemoglobin dissociation curve in Fig. 2. Additionally, in certain cases, such as hyperoxia, it cannot assess oxygenation correctly and has limited resolution [13], [14]. Another noninvasive technique to measure PaO₂ is the transcutaneous partial pressure of oxygen (PtcO₂), which measures blood oxygen diffused through the skin. Changes in PtcO₂ can be directly correlated with changes in PaO₂, as seen in the inset graph in Fig. 2 [13], [15], [16].

Despite the resolution and accuracy that bulky traditional $PtcO_2$ monitors can provide, they do not scale for wearable medical devices. $PtcO_2$ has been traditionally measured with an electrochemical technique that uses Clark electrodes [9]. Due to the insufficient sensitivity of this method, heating is necessary to increase the concentration of O_2 in the gas over the target skin area by increasing the diffusion of O_2 molecules from the blood vessels. In general, this method suffers considerably from the need to heat the skin [18], [19]. Therefore, it is unsuitable for wearable devices. The reasons negatively affecting the feasibility of a $PtcO_2$ wearable with Clark electrodes are as follows:

 designing a heating mechanism on a wearable would significantly increase the device size;

- during continuous monitoring, heating might irritate or even burn the skin under the hotspot; and
- the power consumption of a wearable with a heating mechanism would increase significantly.

This paper presents a novel wearable PtcO₂ monitoring prototype using the lifetime-based luminescent O₂ sensing technique with hardware-software integration. The advantage of the lifetime-based measurement method compared to the intensity-based method was first presented in [20], [21]. However, the resolution of the prototype in the time domain was insufficient to detect changes at the nanosecond level in humans, and therefore human experiments were performed with intensity-based measurements. In [22], researchers presented a custom-designed analog front end (AFE) that implemented a special lifetime estimation algorithm. However, it was not a complete standalone system. Moreover, [22] did not demonstrate human subject tests. In this work, we present a prototype aiming to resolve the above constraints by offering the following improvements:

- the novel system can capture nanosecond changes in lifetime values in humans using the AFE's internal 14-bit analog-to-digital converter (ADC);
- the proposed prototype not only contains an AFE but also a microcontroller unit (MCU) that controls the operation of the entire system and the pre-processing of luminescence data;
- the presence of MCU allows integration of firmware, which is provisioned to automate the entire data processing task in the future making the system suitable for continuous monitoring of transcutaneous oxygen in a wearable form factor.

The significance of this work lies in its successful demonstration of the performance of the proposed prototype using the lifetime measurement technique through testing on human subjects.

The remainder of this manuscript is organized as follows. Section II provides the background on the principles of luminescent O2 sensing and its two measurement methods. In Section III, we elaborate on the architecture of the proposed system in terms of hardware and firmware. Section IV describes the lifetime estimation method for the luminescent optical response. Section V presents measurement results, including power breakdown, gas testbench experiments, and human subject tests. Section VI compares the proposed prototype with existing oxygenation sensors. Finally, Section VII concludes the work.

II. METHODS OF LUMINESCENT OXYGEN SENSING

A blue light-emitting diode (LED), a long-pass emission filter, a photodiode (PD) responsive to red light, and a luminescent sensing film are the essential components of the luminescent oxygen sensing method. When the sensing film is excited by a blue LED with a peak emission wavelength (λ) of 450 nm, the luminophore molecules transition from their ground energy state to a higher energy state. When the luminophore molecules leave this higher energy state, photons with the peak λ of 650 nm are re-emitted and further detected by the PD. The intensity and lifetime (τ) of the re-emitted red light are inversely proportional

to the partial pressure of oxygen (PO_2) since O_2 acts as a quencher when interacting with the luminophore molecules. Therefore, by measuring either the intensity or the lifetime of re-emitted red photons, one can estimate PO_2 [17], [20]. In modern devices, the photocurrent corresponding to the intensity and lifetime of photons is measured by various AFEs [14], [23], [24], [25].

A. Intensity-Based Method

The luminescent intensity contains information about the quantity of re-emitted photons [26]. The quenching effect of O_2 decreases the luminescent intensity proportionally to the number of O_2 molecules in the environment. The method employed to define PO_2 by measuring the luminescent intensity is called the intensity-based method. This method, however, is known not to be robust enough against the changes in optical path and reflections, which negatively affects the accuracy of PO_2 measurements [22], [23].

B. Lifetime-Based Method

After the sensing film is excited, luminophore molecules randomly return to the ground state, emitting photons. A part of the absorbed energy is lost via collision with O_2 molecules. The measured luminescence lifetime is numerically equivalent to a statistical average of this random process [27]. In other words, the strength of quenching, causing a decrease in τ , is proportional to PO_2 [28]. Therefore, the lifetime-based method is used to correlate these two parameters. As it was mentioned in Section I, this method also eliminates the need for heating, but at the same time, requires a high resolution of the analog front end. Compared to the intensity-based method, the lifetime-based method is less sensitive to changes in the optical path and reflections [17], [20], [22]. Therefore, we opted for using the latter measurement method in the proposed prototype to perform human subject tests.

III. SYSTEM ARCHITECTURE

The prototype consists of four primary hardware blocks, illustrated in Fig. 3:

- a power management unit (PMU) responsible for power distribution among other blocks;
- a sensor head that optically excites the film and receives an optical response from it;
- an AFE, connected to the sensor head, which drives the LED and converts the luminescence signal into a digital code; and
- 4) an MCU, on which the host application (firmware) resides. The firmware running on the MCU controls the PMU, configures the AFE, processes the digitized optical data from the AFE, and transmits data to the base station.

A. Hardware

The prototype was implemented on a printed circuit board (PCB), presented in Fig. 4. The current board size is 100 mm by 50 mm, including external connectors on the left and right

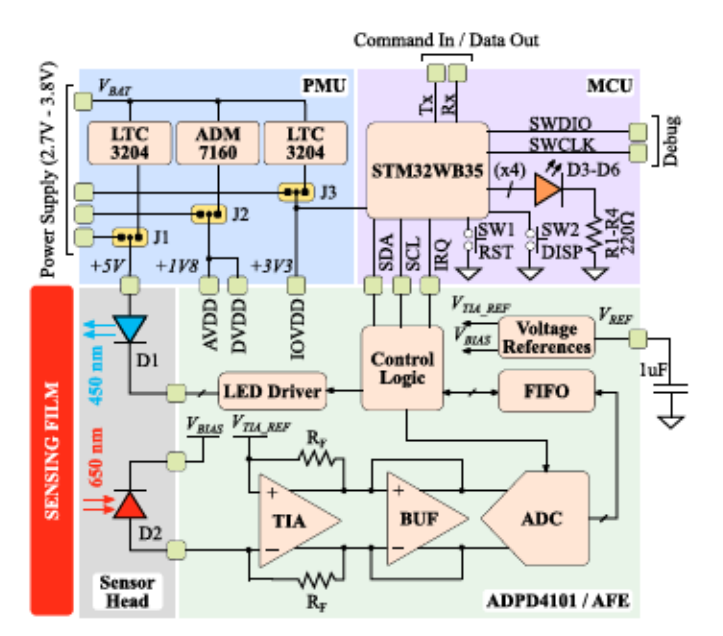


Fig. 3. Block diagram of the proposed prototype for PtcO2 monitoring.

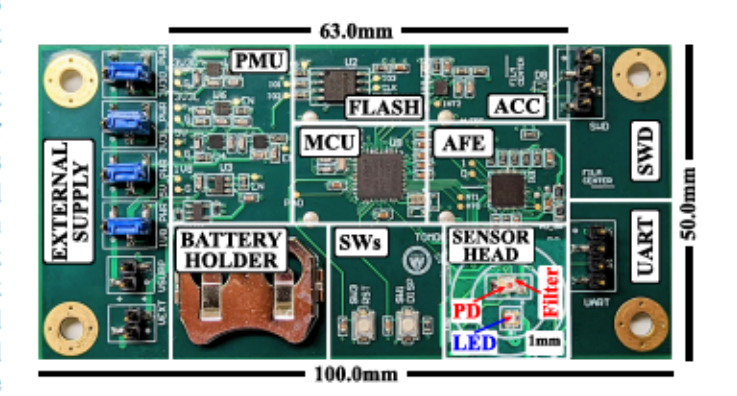


Fig. 4. The top side of the PCB of the oxygen sensor prototype, with an image insert of the sensor head located on the bottom side.

sides of the PCB. The left-side connectors are for the prototype characterization, while the right-side ones are for debugging and communicating with the prototype. In the final prototype, the left-side connectors will be removed and the right-side ones will be lessened to reduce the dimensions of the PCB to 63 mm by 50 mm.

- Power Management Unit: in this prototype, we employed three power rails:
 - a 5 V rail that drives the LED;
 - a 1.8 V rail that powers up both the analog and digital parts of the AFE; and
 - a 3.3 V rail that supplies both the onboard MCU and the input/output (I/O) driver of the AFE.

The reason for using the same supply voltage for the AFE I/O driver and the MCU is to provide the same high logic level for proper communication between these two blocks. Two charge pumps (LTC3204 by Analog Devices Inc. (ADI)) produce stable 3.3 V and 5 V supply voltages, and a low-dropout (LDO) regulator (ADM7160 by ADI) provides a stable 1.8 V supply.

The LDO and charge pumps receive input power from either an external DC power supply or a 3 V lithium coin cell battery [29], [30]. In addition, we have added external connectors (J1 – J3 in Fig. 3) for testing purposes.

- Sensor Head: the sensor head, depicted in Fig. 4, consists of the following four items:
 - a luminescent sensor sensitive to oxygen (Red Eye by Ocean Insight [31]);
 - an LED (LXZ1-PR01 by Lumileds) with a peak wavelength of 450 nm for sensor excitation;
 - a PD (SD019-141-411-R by Advanced Photonix) with an integrated bandpass filter and a responsivity of 0.05 A/W, passing red light with a peak wavelength of 600 nm; and
 - a 500 nm, long-pass optical filter (Everix by Edmund Optics) over the PD active region to further reduce the effect of blue light on lifetime measurements.
- 3) Analog Front End: in previous research, we found that the measured lifetime values for oxygen concentrations in the human-relevant range of 50-150 mmHg were on the order of $10 \mu s$ [20], [32], [33]. Therefore, we aim to have an AFE that can respond to time constants less than 1 μs , which requires a bandwidth of greater than ~ 160 kHz $(\frac{1}{2 \cdot \pi \cdot \tau})$. In order to accurately estimate the lifetime in transcutaneous sensing applications, we need at least three data points on the photon decay curve [20], which requires an ADC with a sampling rate of at least 250 KSPS. To satisfy these requirements, we utilized the ADPD4101 multimodal photometric sensor front end [34] in the proposed system. ADPD4101 provides a 14-bit ADC with resolution ranging from 0.37 to 5.84 nA/least significant bit (LSB) depending on the gain of the transimpedance amplifier (TIA). The sampling rate of the internal ADC is adjustable from 0.5 to 32 MHz based on the sampling method [32]. Moreover, depending on the TIA's gain, the system's input-referred noise (IRN) and signal-to-noise ratio (SNR) range from 0.97 to 10.3 nA _{rms} and from 72 to 76 dB [34], respectively. Also, the TIA's linear dynamic range varies from 4.7 to 72 μ A based on the adjusted TIA gain. Furthermore, ADPD4101 contains four dual-output LED drivers and is capable of measuring the return optical signal on up to four pairs of current inputs combined into two processing and sampling channels [32]. The LED drivers are current sinks, and each output of these drivers can be programmed from 0 to 200 mA with monotonic 1.5 mA increments. Although up to four LED driver outputs can be enabled, there is a limitation of 400 mA in the provided LED current. In addition, the input pairs can be configured as either two single-ended inputs or as a differential pair and connected to one of the channels. This selection is made in certain registers of the ADPD4101. In our system, one single-ended current input is connected to the first channel of ADPD4101. The remaining inputs and the second channel are disabled to reduce power

The linked channel's analog-signal path contains:

- a TIA with an adjustable gain (from 12.5kΩ to 200kΩ) through a programmable feedback resistor (R_F) — transforms photocurrent into a voltage;
- a buffer for passing the TIA's output to an ADC; and
- an ADC for digitizing the analog signal.

To bias the noninverting terminal of the TIA and reverse bias the PD, two voltages, V_{TIA_REF} and V_{BIAS} , have been internally generated. The data sampled by the ADC is written to a first-in-first-out (FIFO) memory buffer.

- Microcontroller: we employed the STMicroelectronics STM32WB35CC MCU for:
 - configuring the AFE to drive the LED;
 - 2) getting the digitized luminescent signal from the AFE; and
 - communicating with a base station (PC) to convey the experimental data.

The MCU is dual-core. The firmware resides on CPU1 (Arm Cortex-M4 CPU). CPU2 (Arm Cortex-M0+ CPU) controls the RF (Bluetooth Low Energy - BLE) subsystem and is disabled in the current prototype. The hardware reset feature is provided to MCU by connecting the SW1 switch to the V_{RESET} pin. We used the Serial Wire Debug (SWD) port to program and debug the MCU. The Inter-Integrated Circuit (I^2 C) bus connects the MCU and ADPD4101 for data exchange. The digitized luminescent data received by the MCU from the AFE's FIFO via I^2 C has been further transmitted via the Universal Asynchronous Receiver-Transmitter (UART) interface to a personal computer (PC) to calculate τ .

B. Firmware

In the proposed PtcO₂ monitoring prototype, the firmware is bare-metal, which means that no real-time or general-purpose operating system (OS) is used. The firmware implements an infinite main loop, also known as the super-loop architecture. Having no OS provides low-level hardware control and reduces memory and power overheads.

In the firmware, initialization routines are executed before an infinite loop, which contains the system's main tasks except for interrupt service routines (ISRs), also referred to as interrupt handlers. There are two handlers for hardware interrupts (ISR 1 and ISR 2) and one timer interrupt (ISR 3). ISR 1 is triggered when the AFE generates a falling edge on its GPIO0 pin (signal IRQ, or interrupt request, in Fig. 3), indicating that its FIFO buffer contains the number of samples predefined in the ADPD4101's configuration file. ISR 2 activates a system timer to debounce the display button SW2. ISR 3 is called when the system timer's period has elapsed.

Fig. 5 shows a flowchart of the primary firmware logic. During the initialization phase, the MCU and its modules (memory, system clock, communication interfaces, input/output ports, etc.) are configured. Then, the MCU establishes a connection with the AFE via I² C. After that, the MCU loads a configuration file into the AFE and puts the AFE into GO mode (sampling). Next, the main loop checks the status of the data-ready flag set by ISR 1. If the flag is set, it puts the AFE into IDLE mode (standby) and reads out the data available in the AFE's FIFO. When the data is read, the MCU parses it, stores the parsed values into an array, and updates the variables controlling the parsing of the following data sets. After that, it puts the AFE back into GO mode. The main loop stops its operation after a given number of decay curves have been collected and averaged to produce the final result.

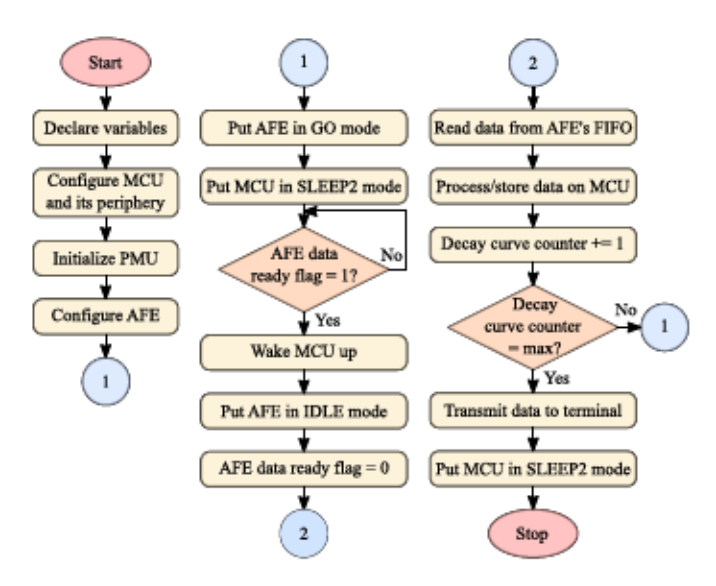


Fig. 5. The flowchart of the main firmware logic.

To reduce current consumption, the MCU is put into STOP2 low-power mode while waiting for data from the AFE. The integrated real-time clock (RTC) peripheral is used to wake the MCU up with a period of 10 ms, corresponding to the timeslot period of the AFE [35], [36], [37]. After the RTC period has elapsed, the MCU wakes up and checks the data-ready flag set by ISR 1. If the flag has been set, the MCU processes the data received from the AFE and returns to the low-power mode. Otherwise, the MCU enters STOP2 mode and waits until the next RTC period ends. These steps repeat until the pre-defined number of decay curves has been collected.

IV. LIFETIME ESTIMATION TECHNIQUE

To extract the lifetime information of the luminescent signals, we employed a sampling technique called impulse response (IR) mode. The lifetime estimation process includes three primary steps:

- setting up the necessary parameters for ADPD4101, defined in the MCU's firmware, to enable lifetime measurements in IR mode;
- sampling a decay curve; and
- processing of the captured decay curve to estimate lifetime

A. Impulse Response Mode

ADPD4101 manages the control of excitation sources and the measurement of sensor readings. An intrinsic controller, configured by MCU, handles ADPD4101's operation by creating all timing information required to generate time slots. In the IR mode, one time slot is periodically activated, as illustrated in Fig. 6. The time slot is preceded by a wake-up interval, where the analog circuitry turns on and gets stabilized before the start of the sampling process. At the beginning of the time slot, there is a preconditioning interval, where the PD's cathode is pulled to an internally generated potential to reverse bias the PD. The preconditioning period is followed by a pulse offset interval, after

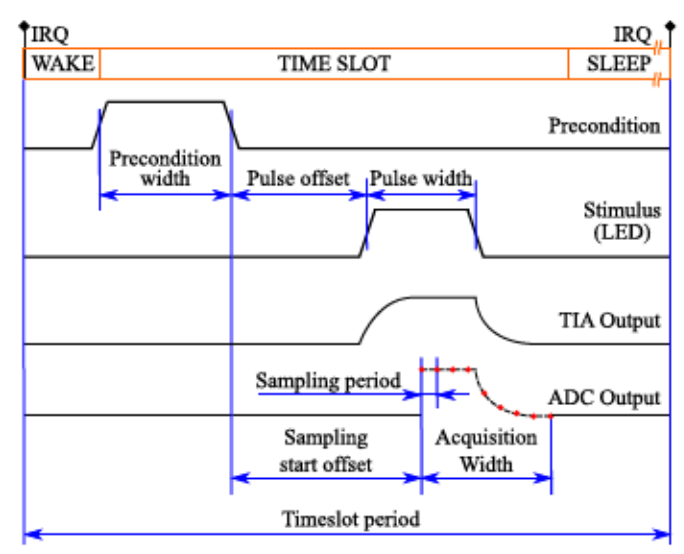


Fig. 6. Timing diagram of the impulse response (IR) mode.

which the blue LED is pulsed to excite the luminescence-sensing film. Then, the film's optical response, captured by the PD, is recorded. The recorded TIA output closely matches the photon decay curve. Further, the ADC samples the TIA output and converts the voltage to a total number of the LSBs, completing the data acquisition in the IR mode. Finally, ADPD4101 enters an ultra-low-power mode for the duration of the sleep period.

B. Parameter Settings

In IR mode, several parameters need to be set, according to Fig. 6:

- the precondition width,
- the LED pulse width,
- the LED pulse offset relative to the end of the preconditioning interval,
- 4) the LED current,
- 5) the ADC sampling period,
- the ADC sampling start offset relative to the end of the preconditioning interval,
- the data acquisition width, and
- the TIA gain.

These parameters have specific register addresses in ADPD4101, and their values are configurable in the MCU's firmware. The precondition width and the pulse offset intervals have no direct impact on system performance. Therefore, we set their default values to $8\,\mu s$ and $16\,\mu s$, respectively, as specified in ADPD4101's datasheet.

However, the remaining parameters directly influence the system performance and, therefore, should be set appropriately. The LED pulse width and current significantly impact the overall power consumption, as LEDs are among the most power-hungry parts of a wearable device. Therefore, reducing these two values is highly desirable. On the other hand, to obtain accurate measurements with a good signal-to-noise ratio, the LED pulse must be long enough and the LED current must be high enough to excite enough luminophore molecules in the sensing film.

Based on our previous findings in [32], [33], we set the LED pulse width and LED current to $100 \,\mu s$ and $250 \,\text{mA}$ to achieve a good balance between power consumption and measurement accuracy.

The acquisition width defines the time interval we collect samples for a decay curve, while the sampling period of the ADC determines the distance between samples and the number of samples collected in the given acquisition width. Finally, ADC's sampling start offset determines the start of the acquisition window. In short, these three parameters — the acquisition width, the sampling period, and the sampling start offset — determine the number and position of samples on the decay curve, affecting the accuracy and precision of lifetime estimation. Therefore, we set the sampling period to $2\,\mu s$ (the minimum achievable sampling period) and the acquisition width to $128\,\mu s$. We started sampling $10\,\mu s$ before the end of the LED pulse to capture the entire decay curve and to estimate the decay time accurately.

Finally, the TIA gain setting should be thoroughly considered, because a high TIA gain is desirable to detect low input currents in the case of high oxygen concentration and to improve the ADC resolution. However, at the same time, a high TIA gain may saturate the AFE and contribute to power consumption. Considering all these tradeoffs, we chose the TIA gain as $100~\mathrm{k}\Omega$ to aim for a balance between these requirements. In addition, to reduce noise in the final data, we repeated measurements $100~\mathrm{times}$ and computed a point-wise average of each decay curve we measured. This averaging produced a cleaner decay curve and allowed a more precise decay constant measurement. The memory array was statically allocated and equal to $\sim 12.7~\mathrm{KB}$ (100 decay curves, 65 data points per decay curve, and 2 bytes per data point), which was $\sim 5\%$ of the total Flash memory available on the STM32WB35CC MCU.

C. Lifetime Extraction Process

We processed the ADC data received via UART in MATLAB. To prevent the blue light's effect on the lifetime estimation, we measured the LED-PD coupling and stored the data (when the optical path was empty with no luminescent film present) for different LED currents ranging from 50 mA to 400 mA in 50 mA steps. We further subtracted these dark data corresponding to the configured LED current from the luminescence data recorded with the film. To extract the lifetime from the measured decay curve, we performed an exponential regression in MATLAB on the samples collected $4\,\mu s$ after the end of the LED pulse; we waited for the blue light's fading to avoid its residual artifacts based on our earlier experiments [33]. This pre-processed ADC data is closely related to the photon decay curve and can be represented mathematically as follows:

$$y(t) = A \cdot e^{-t/\tau} + B, \qquad (1)$$

where y(t) represents the decay curve, while A, τ , and B are the unknown coefficients.

To perform exponential regression on the collected ADC data, we use the *fitnlm()* function of MATLAB [38]. This function requires three main parameters:

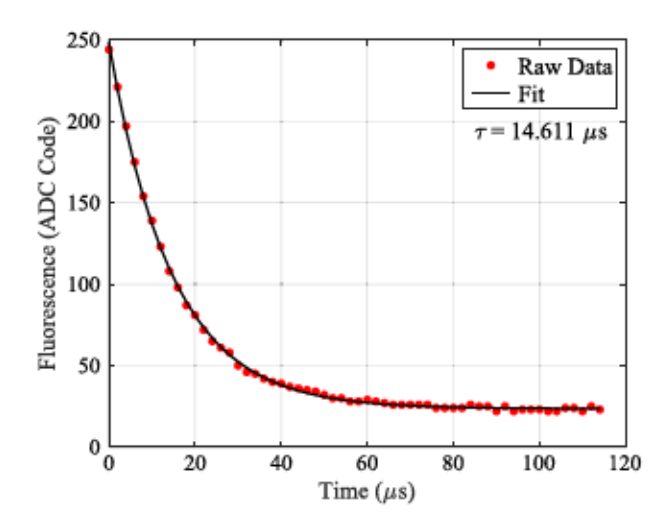


Fig. 7. Exponential regression of luminescent data for lifetime extraction.

- a dataset array that contains predictor x and response y, which, in our case, represents time and ADC data, respectively;
- 2) a model function $f(x, \beta)$ that represents the type of fit applied to the dataset (in our case, (1)); and
- an array β₀ that includes the initial guesses of coefficients of the model function.

Based on these parameters, the fitnlm() function employs the Levenberg-Marquardt nonlinear least squares algorithm to obtain the model function's optimum coefficients, which minimizes the sum of the squared deviations $S(\beta)$ from the response variable [39]. In general, the algorithm iteratively follows four main steps [39]:

1) update β_0 with $\beta_0 + \delta$ by solving the following equation for δ :

$$\delta = (J^T J + \lambda I)^{-1} J^T (y - f(x, \beta_0)), \tag{2}$$

where J is the Jacobian matrix containing the gradient of $f(x, \beta)$ with respect to β , λ is the damping factor, and I is an identity matrix;

2) calculate $S(\beta)$ with the updated version of β_0 by using the following equation:

$$S(\beta_0 + \delta) = \sum_{i=1}^{n} (y_i - f(x_i, \beta_0) - J_i \delta)^2,$$
 (3)

where n is the size of arrays;

- compute the difference between S(β₀ + δ) and previous value of S(β); and
- update λ based on this difference.

This algorithm continues until a certain convergence criterion is met or the number of iterations exceeds a predetermined limit. Fig. 7 presents an example of exponential regression and lifetime estimation applied to raw data obtained under atmospheric conditions with the use of the AFE's parameters.

The use of MATLAB in this iteration of our system was sufficient for our goal of conducting a small, laboratory-based study on human subjects to verify the prototype's efficiency in registering changes in the amount of transcutaneous oxygen diffusing through the skin with the lifetime-based measurement algorithm. In the current prototype, the data processing on the MCU includes traversing through the AFE's FIFO content, parsing decay values, and packaging them for further transmission to a PC.

V. MEASUREMENT RESULTS

This section presents the measurement results of three distinct sets of experiments. First, we carried out power breakdown experiments to calculate the power consumption of each subsystem. Second, we conducted a gas testbench experiment to evaluate the prototype's performance with various gas ratios. Finally, we performed a small human subject testing on three volunteers by following the test procedures described in the relevant subsection.

A. Power Breakdown

The MCU operates in two modes:

- RUN mode, in which the necessary data for lifetime measurements are processed, and
- STOP2 mode, in which the MCU enters a low-power state and waits for an interrupt from the RTC to wake up.

To calculate the total average current consumed by the prototype, we repeatedly measure the current consumption in each mode. For this purpose, we developed a MATLAB script controlling a DC power supply connected to a PC via a USB cable. On the prototype board, the DC source provides 3 V to the regulators, supplying power for each power rail, as illustrated in Fig. 3. For repeated current readings, we reset the MCU every 24 seconds, allocating eight seconds for RUN mode and 16 seconds for STOP2 mode, for 30 minutes. We employ the following equation to calculate the total average current consumption:

$$I_{avg} = \frac{I_{run} \cdot t_{run} \cdot N + I_{stb} \cdot t_{stb} \cdot M}{t_{run} \cdot N + t_{stb} \cdot M},$$
 (4)

where I_{avg} is the total average current consumption, I_{run} is the current consumption in RUN mode, t_{run} is the duration of RUN mode, and N is the number of times the prototype entered RUN mode in 30 minutes. I_{stb} , t_{stb} , and M are corresponding parameters for STOP2 mode.

We calculate the total average current consumption by excluding the consumption of a particular subsystem (e.g., the AFE, the blue LED, or the MCU). We follow the same procedure for each measurement to record data. Then, we utilize (4) to estimate total average values. Finally, we solved the following matrix equation to calculate the average current values of each subsystem with these values:

$$\begin{bmatrix} 0 & 1 & 1 \\ 1 & 0 & 1 \\ 1 & 1 & 0 \end{bmatrix} \begin{bmatrix} \langle I_{AFE} \rangle \\ \langle I_{LED} \rangle \\ \langle I_{MGU} \rangle \end{bmatrix} = \begin{bmatrix} I_{\Sigma_1} \\ I_{\Sigma_2} \\ I_{\Sigma_2} \end{bmatrix}, \quad (5)$$

where $\langle I_{\rm AFE} \rangle$, $\langle I_{\rm LED} \rangle$, and $\langle I_{\rm MCU} \rangle$ are the unknown average consumed currents of AFE, blue LED, and MCU, respectively.

The calculated average current consumption, excluding the consumption of AFE, blue LED, and MCU, is represented by the variables I_{Σ_1} , I_{Σ_2} , and I_{Σ_3} , respectively. Finally, we gave the

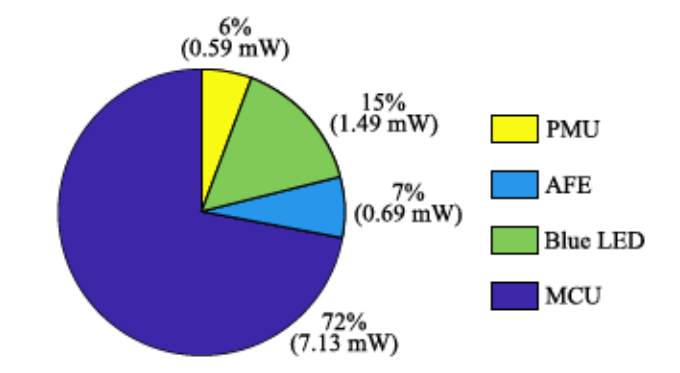


Fig. 8. Power consumption breakdown.

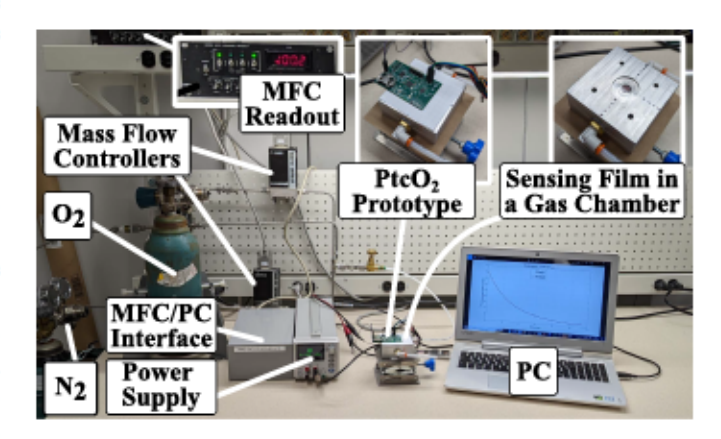


Fig. 9. Annotated gas experiment testbench. Adapted from [33].

breakdown of the power consumption for each block in Fig. 8. The measured total average power consumption of the prototype is 9.9 mW, with the MCU consuming four-fifths of the power and running in STOP2 mode.

B. Gas Testbench Experiment

A gas chamber experiment was designed to examine the prototype's response to various gas ratios. In the gas chamber setup, illustrated in Fig. 9, the luminescent film is located inside an aluminum gas chamber while the prototype is placed above the chamber. The sensor head's center is aligned with the film's center. To adjust PO₂, oxygen (OX UHP20 by Airgas) and nitrogen (NI UHP80 by Airgas) are mixed at a specific mass flow rate. Two MKS 1179A12CS1BV mass flow controllers (MFCs) and one MKS 247 mass flow control (power supply and readout) unit adjust the mass flow rate of nitrogen and oxygen. The MFC/PC interface is employed to operate the entire system from a PC.

To show the robustness of the lifetime-based method against optical path changes, we performed a gas sweep experiment with two different LED drive strengths, 150 mA and 250 mA. The reason behind this choice was to imitate a case like in [20], where the effect of different optical paths is modeled by modulating the PD current with different LED drive powers. We adjusted the partial pressure of oxygen in a controlled environment using predetermined steps. The flow rate of nitrogen in the system was initially set to 100 standard cubic centimeters per minute (sccm),

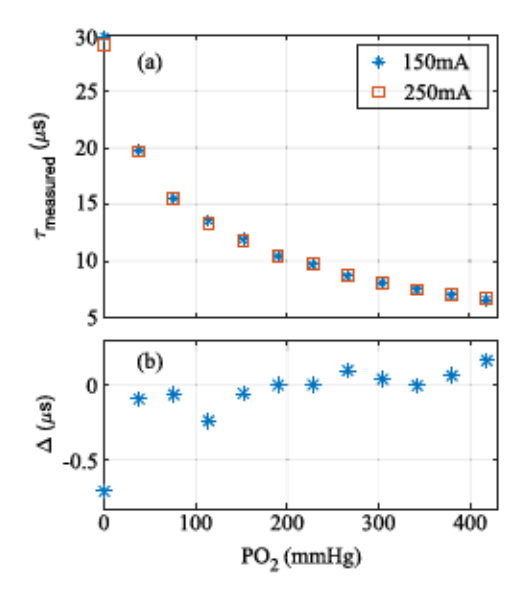


Fig. 10. Gas sweep in the range of 0–418 mmHg: (a) lifetime values for two distinct LED currents and (b) a difference between measured lifetimes. Adapted from [33].

while the flow rate of oxygen was set to 0 sccm. After the flow of both gases stabilized, the lifetime measurement was taken. Then, the nitrogen flow rate was reduced to 95 sccm, while the oxygen flow rate was increased to 5 sccm, and we re-measured the lifetime. These measurements were continued until the oxygen flow rate reached 55 sccm and the nitrogen flow rate reached 45 sccm.

In this way, PO_2 ranged from 0 to 418 mmHg in 38 mmHg increments, covering the human-related range, as depicted in Fig. 10-a. Accordingly, the recorded lifetime varied from $30\,\mu s$ to $6.6\,\mu s$ for PO_2 , corresponding to 0 to 418 mmHg. Furthermore, Fig. 10-b shows a continuous inaccuracy of less than 0.25 μs between recorded lifetime readings of the same PO_2 values, except in the 0 mmHg case, where the lifetime value is the highest. As a result, these findings agreed with the literature that the lifetime-based technique should be resistant to changes in the optical path [20], [22] since the current intensity detected on the PD has no significant effect on the PO_2 readings.

To demonstrate the transient lifetime response of the proposed prototype, we changed the PO_2 using a similar increment size and following the same procedure. In each step, lifetime measurements were taken every 3 seconds over a 3-minute period. The results of the transient lifetime measurement are presented in Fig. 11. The prototype was responsive to the changes in the lifetime value, corresponding to the step increases in PO_2 . The measured lifetime ranged from $32\,\mu s$ to $9.5\,\mu s$ for PO_2 ranging from 0 to 418 mmHg. We believe the subtle difference in the two gas sweep tests was caused by the aging of the film, as there were three months between those measurements.

C. Human Subject Tests

To investigate the prototype's performance, we conducted a small experiment on human subjects. This laboratory-based study included three healthy volunteers (two males and one

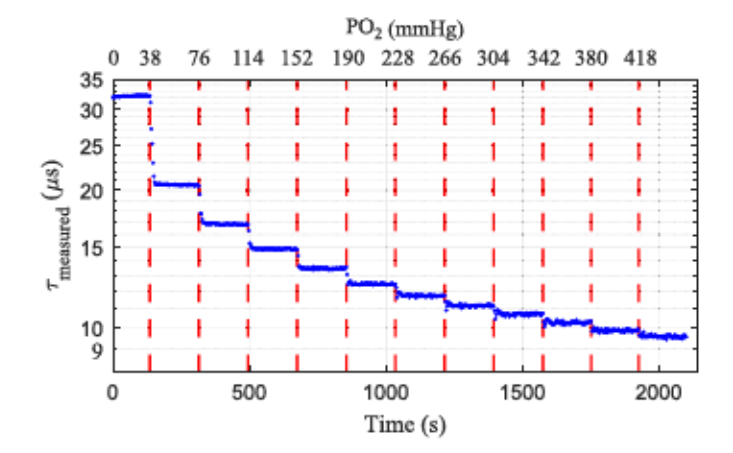


Fig. 11. Transient response of the sensing film to the step changes in PO₂ (the red dashed lines indicate the times when the value of PO₂ increased by 38 mmHg, as shown in the top of the graph).

female). Each volunteer gave verbal consent. The Worcester Polytechnic Institute – Institutional Review Board (WPI–IRB) examined and approved the experimental protocol. All research team members received training through the Collaborative Institutional Training Initiative (CITI) [40] on responsible research conduct and human participation in biomedical research. This ensured the compliance with procedures and the familiarity of researchers with the various international and country regulations/codes and standards applicable to the ethical conduct of human subjects research, including the Declaration of Helsinki [41]. The tests were performed at the fingertips and the forearm of volunteers. We followed two distinct methods, namely pressure-induced arterial occlusion and hypoxic gas delivery, to modulate the partial pressure of O2 diffusing through the skin to examine the prototype's response to biological changes in the body.

The validation of the system was conducted in an 8 m² room at an average air temperature of ~ 25 °C in a building located at an altitude of 163.8 m above sea level (corresponding to the air pressure of \sim 760 mmHg and O_2 concentration of \sim 20.9%) [42], [43], [44]. Test subjects had different ages, gender, and skin tones to improve the accuracy of the data collection protocol and minimize measurement bias among test subjects of different races and ethnicities [45]. The volunteers were asked not to eat or drink for 3-4 hours before the experiment began in order to get stable levels of oxygen. To provide a restful environment, test subjects sit in a chair in a comfortable position. Based on our previous experiments, the position of the hand was adjusted so that the subjects did not experience numbness in their limbs/fingers. [20] identified that the measured lifetime of the red light emitted by the luminescent film (τ) is independent of the humidity levels (including perspiration). At the same time, it revealed that the measured τ is dependent on the surrounding temperature. Before and after each experiment, we measured the test subject's body part's temperature with a non-contact infrared thermometer (ITH93 by ConairCare) cleared by the U.S. Food and Drug Administration (FDA). The skin temperature in the areas of interest remained relatively constant in a narrow range

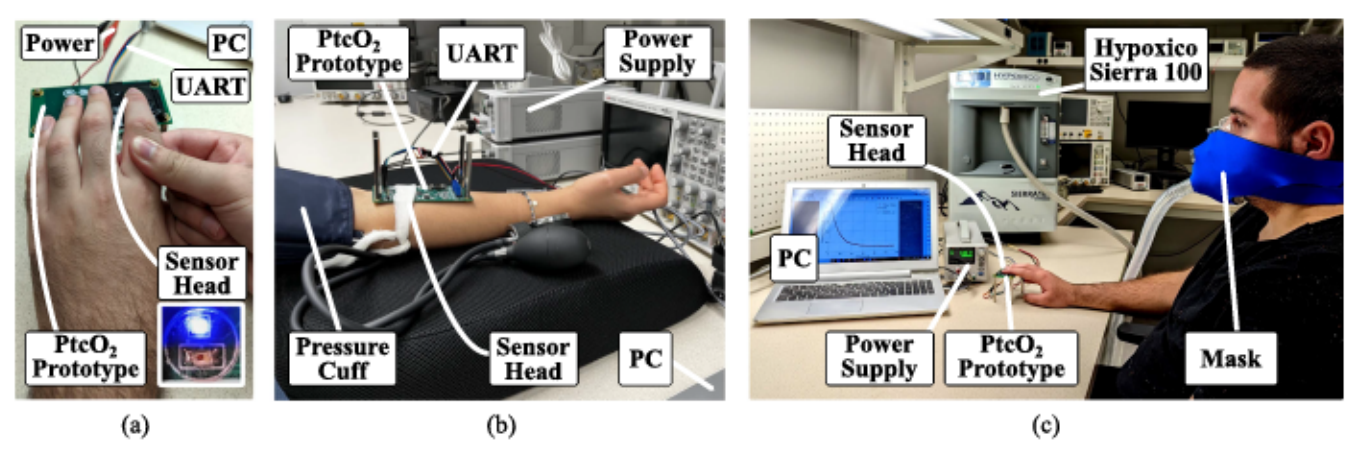


Fig. 12. Experimental setups for human tests: (a) occlusion caused in the index finger, (b) occlusion caused in the hand, and (c) hypoxia.

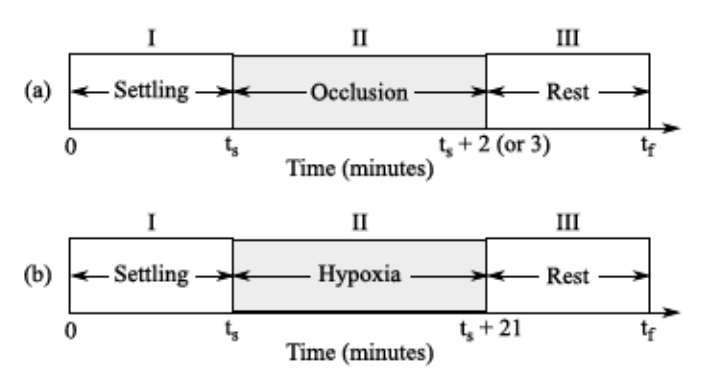


Fig. 13. Timing diagrams of the test procedures for (a) an occlusion event and for (b) a hypoxia event.

of $\sim 36~^{\circ}\text{C}$, and therefore its effect on the measurement results was not considered.

Three experimental setups were prepared as depicted in Fig. 12. In all setups, the luminescent film is attached to acrylic glass and placed directly on top of the sensor head. In experiments involving fingertips, a volunteer places their fingertip on the luminescent film. In experiments involving the forearm, the prototype and the luminescent film are placed on the volunteer's forearm, as illustrated in Fig. 12-b. To decrease the blood circulation through occlusion, either the index finger can be clenched by the fingers of the opposite hand, as shown Fig. 12-a, or a pressure cuff can be placed on the upper arm, as displayed in Fig. 12-b. In the latter, the cuff pressure should be inflated to 180 mmHg to induce arterial occlusion, resulting in a decrease in the volunteer's PtcO₂ [20].

To induce hypoxia, an altitude generator (Sierra 100 by Hypoxico) [46], hereafter referred to as HS100, with a mask on the volunteer's face was employed, as demonstrated in Fig. 12-c. HS100 reduces the PO_2 in the air contained in its reservoir and inhaled by the volunteer. The reduced O_2 intake causes an overall decrease in PaO_2 in the body, leading to a decrease in the volunteer's $PtcO_2$.

We followed specific testing procedures whose timing diagrams are presented in Fig. 13. We repeatedly measured the lifetime every 7 seconds. For occlusion, the testing procedure illustrated in Fig. 13-a is divided into three zones. Zone I is the settlement phase where the oxygen in the sensing film reaches equilibrium with the oxygen diffusing through the skin. The duration of this zone is denoted as \mathbf{t}_s . After stabilization, we take the mean of the last ten lifetime values as the base value. Zone II is the occlusion phase, where we apply arterial occlusion. This zone lasts two or three minutes, depending on the experiment. During the occlusion phase, as $PtcO_2$ decreases, the lifetime value increases. Finally, during the resting phase – Zone III – the occlusion is removed and blood flow is restored to the base value. Similar to Zone I, the duration of Zone III, is expressed as $\mathbf{t}_f - t_s = (2 \text{ or } 3)$.

A similar timing diagram of the hypoxia-induced event is displayed in Fig. 13-b. As in the case of occlusion, we record the base lifetime value after the stabilization of oxygen in the luminescent film in Zone I. The duration of this phase is denoted as \mathbf{t}_s . In Zone II, we change the PO₂ in the reservoir from 18.1% to 15.1% in seven intervals, each taking three minutes. Finally, in Zone III, we remove the mask and let the volunteer breathe the ambient air. Eventually, we expect the PaO₂ in the blood to return to its original value before the modulation. In addition, the duration of Zone III is expressed as $\mathbf{t}_f - t_s - 21$.

We conducted the first occlusion test on the first volunteer from the finger, as illustrated in Fig. 12-a, and followed the procedure presented in Fig. 13-a. Fig. 14 demonstrates the results of this test. The lifetime stabilized around 13.6 μ s in five minutes. Following stabilization, arterial occlusion was applied for three minutes, and the lifetime increased to 14.6 μ s as PtcO₂ dropped. After releasing the pressure on the finger, the lifetime immediately began to decrease in Zone III, lasting five minutes, as oxygenated blood began to flow. Eventually, the lifetime stabilized at around 13.8 μ s. The differences between four adjacent example τ values, where $\Delta_1 = 6.6585$ ns, $\Delta_2 = 1.7789$ ns, and $\Delta_3 = 13.6943$ ns, are displayed in the inset graph in Fig. 14 to illustrate that our system can resolve variations in the lifetime data on the order of units of nanoseconds.

The second occlusion test was carried out on the forearm of the second volunteer following the procedure in Fig. 13-a.

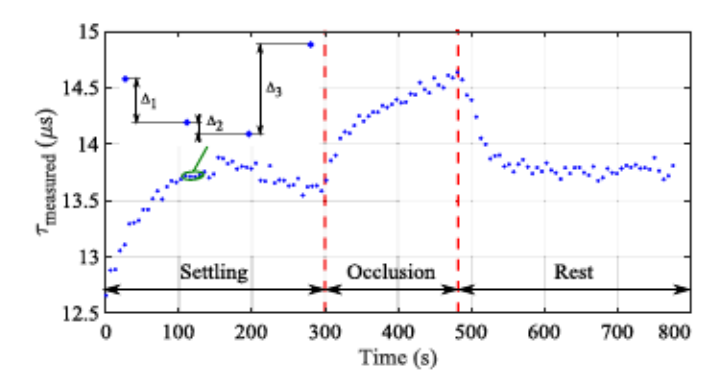


Fig. 14. Measured lifetime at the fingertip during an occlusion event for volunteer 1. The inset image exhibits the example differences in τ values between adjacent data points, where $\Delta_1=6.6585\,\mathrm{ns},\,\Delta_2=1.7789\,\mathrm{ns},\,\mathrm{and}\,\Delta_3=13.6943\,\mathrm{ns}.$

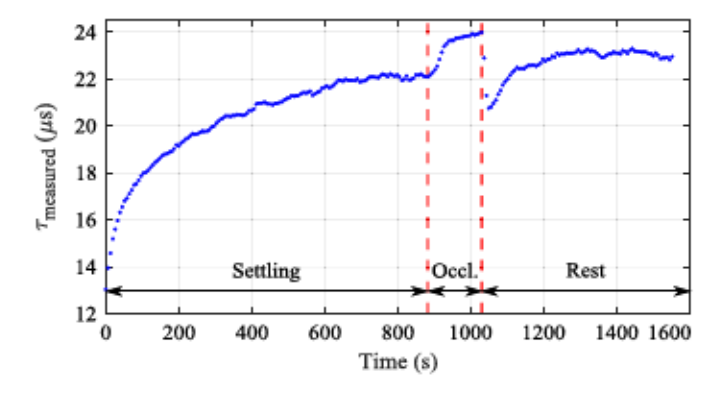


Fig. 15. Measured lifetime at the forearm during an occlusion event for volunteer 3 (where Occl. denotes the occlusion phase).

Arterial occlusion was induced using a pressure cuff and the measurement was taken from the forearm, as depicted in Fig. 12-b. The result of this experiment is presented in Fig. 15. The lifetime stabilized at around $22.1\,\mu s$ in 15 minutes. An increase in the lifetime to $24\,\mu s$ was observed after preventing the influx of oxygenated blood for two minutes in Zone II. After releasing the pressure on the cuff, the lifetime dropped sharply before returning to slightly above the base value. This rapid drop in lifetime may be explained by the fact that when the pressure on the forearm is released, there is a rush of oxygenated blood into the forearm, increasing PaO₂ above the value before occlusion. The lifetime stabilized at around $23\,\mu s$ after blood flow was restored, slightly higher than the base value.

Finally, we conducted the hypoxia test on the third volunteer from the fingertip, as illustrated in Fig. 12-c, following the procedure presented in Fig. 13-b. Fig. 16 demonstrates the results of this test. In Zone I, the stabilization of the lifetime took nine minutes, and it settled around the lifetime of $12.7 \mu s$. During the hypoxic gas delivery, the lifetime gradually increased to $13.6 \mu s$ in 21 minutes. It should be noted that the hypoxic gas delivery changed the oxygen amount in the whole body, leading to a slow and delayed metabolic response. After removing the mask in Zone III, an increase in the lifetime to $14.1 \mu s$ was observed due to the body's delayed response to the changes.

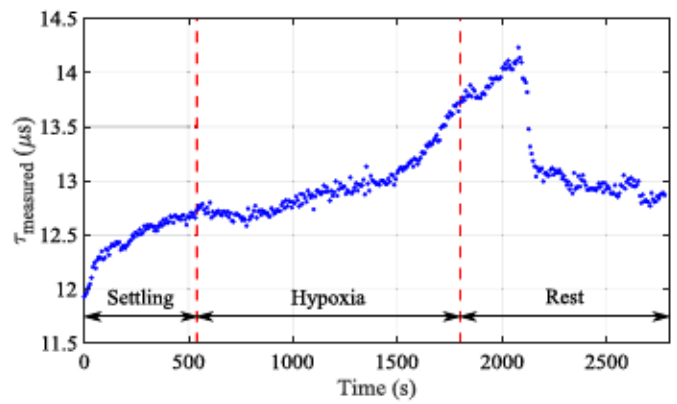


Fig. 16. Measured lifetime on the fingertip during a hypoxia event for volunteer 2.

Then, the lifetime started to decrease and stabilized at around $12.8 \mu s$, over the course of 16 minutes.

Human subject tests revealed that the current prototype could resolve even slight (on the order of several units of nanoseconds) in the lifetime data with the AFE having a 14-bit ADC on board. These tests also demonstrated that the prototype responded to changes not only in gas testbench experiments but also in humans with the modulation of actual biological events, such as pressure-induced occlusion and hypoxic gas delivery. While studying person-to-person variations was outside the scope of this work, with these small tests, we could successfully verify the functionality of the proposed prototype in three volunteers. It is also important to note that the PtcO₂ values will differ depending on the measurement location and from person to person, as the amount of blood running below the skin (and accordingly, the amount of transcutaneous oxygen) varies.

VI. COMPARISON WITH EXISTING DEVICES

The proposed prototype for transcutaneous oxygen sensing was compared to several recently reported oxygenation sensors, including PtcO₂ and SpO₂. We summarize the results of this analysis in Table I, outlining the main characteristics and advantages compared to the state-of-the-art sensors. Our prototype — a miniature monitor capable of detecting the global and local modulation of oxygen in the human body through pressure-induced arterial occlusion and hypoxic gas delivery events — is based on a noninvasive lifetime-based measurement technique. The lifetime data can be captured at high resolution with the internal 14-bit ADC of the AFE, enabling our systems to resolve variations in the lifetime data on the order of units of nanoseconds, which is superior compared to previously published works [20], [23].

The systems presented in [20], [48] use the intensity-based technique as a sensing method. In [20], the experiments found that the intensity levels varied by $\sim 28.5\%$ depending on the LED driving strength, and variations in the lifetime values changed only from -2% to 8% in the whole range when using the lifetime-based technique. In contrast, this work demonstrated even better results for the lifetime-based technique as the lifetime

No

Parameters	[20] 2021	[22] 2022	[25] 2021	[47] 2019	[48] 2018	This Work 2023
Publisher	IEEE TBioCAS	ESSCIRC	Nat. Biotechnol.	IEEE TBioCAS	ACM AMI	IEEE TBioCAS
Sensor Type	$PtcO_2$	$PtcO_2$	$PtcO_2$	SpO_2	$PtcO_2$	$PtcO_2$
Supply Voltage (V)	2.2	1.8	1.2	0.6 - 1.2	7.5	3.0
Max. PD Current (μA)	3	N/A	N/A	75	10	12
Transimpedance Gain	$1 \text{ M}\Omega$	2 pF	N/A	$10 \text{ k}\Omega - 1 \text{ M}\Omega$	N/A	$12.5 \text{ k}\Omega - 200 \text{ k}\Omega$
λ of LED (nm)	453	450	460	IR / Red	550	450
λ of PD (nm)	600	650	618	N/A	535	600
Power Consumption (mW)	9	0.835	0.15	0.326*	N/A	9.9
Sampling Rate (SPS)	N/A	5 M‡	360	32 k	N/A	$0.5 \text{ M}^{\dagger} - 32 \text{ M}^{\ddagger}$
PO ₂ Range (mmHg)	0 - 418	0 - 228	0 - 150	N/R	N/A	0 - 418
PO ₂ Error (mmHg)	6.1*	2.2	N/A	N/R	N/A	5.4
Testing	HT	None	AT	None	HT	HT
O2 Sensing Technique	Intensity	Lifetime	Phase	N/R	Intensity	Lifetime

TABLE I
COMPARISON OF PERFORMANCE PARAMETERS OF OXYGENATION SENSORS

Note: *calculated from the original paper. †- nominal. : + maximum. N/A - not addressed. N/R - not relevant. HT - human tests. AT - animal tests.

Yes

values differed between -1.8% and 2.4%. Although the system described in [22] employs the lifetime-based technique, it only consists of an AFE and does not show any human subject test result, while our system contains an MCU that controls the entire system in addition to an AFE. Further, we tested our prototype on humans. The system proposed in [25] requires surgical implantation, making it invasive. The device introduced in [47] measures oxygenation using SpO₂, which is a distinct oxygenation parameter and employs a different sensing method. Unlike SpO₂, the measurement technique used in this prototype has a direct correlation with changes in PaO2, as explained in Section I. The system presented in this work is able to measure in full range from 0 to 418 mmHg compared to [22], [25]. Lower power consumption values were reported in [22], [25], [47] because those systems were designed on small node integrated circuits, operating at lower supply voltages. The power consumption of this prototype is comparable with [20], in which the LED is driven by an external function generator and the onboard MCU is not used. The system proposed in [22] samples at a faster rate compared to this work. However, our prototype is able to sample with a period of up to 31.25 ns using a sampling method called single-sided integration mode (SSI) with the cost of more power consumption [32].

Invasiveness

In addition, compared to [20] and [48], the prototype proposed in this work has a wider input dynamic range, allowing the TIA to pass more PD current before it saturates and, therefore, to process a wider range of luminescence signals. The work reported in [47] delivered a greater input dynamic range because it included a DC cancellation current weighted digital-to-analog converter at the system input. As far as we are aware, our device is the first of its type to perform human subject tests using the lifetime-based method compared to the human subject tests done in [20], [48], employing the intensity-based method.

VII. CONCLUSION

This work presented a novel prototype of a wearable for noninvasive transcutaneous oxygen monitoring based on a lifetime measurement technique. We used a special analog front end — ADPD4101 by ADI — for sensor readings. To record luminescence data in the form of a photon decay curve, we utilized a sampling method called impulse response mode. We report average power consumption of 9.9 mW. In a gas sweep experiment, we confirmed that changes in the optical path do not significantly affect the lifetime-based technique. Then, in a transient gas experiment, we demonstrated that the prototype is capable of measuring the partial pressure of oxygen varying from 0 to 418 mmHg, covering the human-related range with a resolution of several units of nanoseconds. Finally, we performed a small, laboratory-based study to verify the system's operation on humans. In this study, we applied hypoxic gas delivery and pressure-induced occlusion to volunteers to change the amount of transcutaneous oxygen diffusing through the skin. We read the measurements from the volunteers' fingertips and forearms. The results of these tests confirmed that the prototype successfully resolved the nanosecond variations in the lifetime data, indicating that the device could detect arterial occlusion and hypoxic gas delivery events.

No

No

REFERENCES

- A. Nag, S. C. Mukhopadhyay, and J. Kosel, "Wearable flexible sensors: A review," *IEEE Sensors J.*, vol. 17, no. 13, pp. 3949–3960, Jul. 2017.
- [2] T. Weil and S. Murugesan, "IT risk and resilience-cybersecurity response to COVID-19," IT Professional, vol. 22 no. 3, pp. 4–10, May/Jun. 2020.
- [3] U. Guler, I. Costanzo, and D. Sen, "Emerging blood gas monitors: How they can help with COVID-19," *IEEE Solid-State Circuits Mag.*, vol. 12, no. 4, pp. 33–47, Nov. 2020.
- [4] S. Allen, "2020 US and global health care outlook," *Deloitte*, 2020. Accessed: Apr. 22, 2021. [Online]. Available: https://www2.deloitte.com/us/en/pages/life-sciences-and-health-care/articles/global-health-care-sector-outlook.html#
- [5] J. E. Hollander and B. G. Carr, "Virtually perfect? Telemedicine for COVID-19," New England J. Med., vol. 382, no. 18, pp. 1679–1681, Apr. 2020.
- [6] T. B. Tufan et al., "An infra-red-based prototype for a miniaturized transcutaneous carbon dioxide monitor," in *Proc. IEEE 43rd Annu. Int. Conf. Eng. Med. Biol. Soc.*, 2021, pp. 7132–7135.
- [7] I. Costanzo et al., "Respiratory monitoring: Current state of the art and future roads," *IEEE Rev. Biomed. Eng.*, vol. 15, pp. 103–121, 2022.

- [8] T. B. Tufan and U. Guler, "A fluorescent thin film-based miniaturized transcutaneous carbon dioxide monitor," in *Proc. IEEE Biomed. Circuits Syst. Conf.*, 2021, pp. 1–5.
- [9] J. W. Severinghaus et al., "Blood gas analysis and critical care medicine," Amer. J. Respir. Crit. Care Med., vol. 157, pp. S114—S122, Apr. 1998.
- [10] F. B. Ahmad and R. N. Anderson, "The leading causes of death in the US for 2020," *Jama*, vol. 325, no. 18, pp. 1829–1830, 2021.
- [11] M. S. Shiels et al., "Leading causes of death in the US during the COVID-19 pandemic, Mar. 2020 to Oct. 2021," *JAMA Intern. Med.*, vol. 182, no. 8, pp. 883–886, 2022.
- [12] S. Park and S. Jayaraman, "Enhancing the quality of life through wearable technology," *IEEE Eng. Med. Biol. Mag.*, vol. 22, no. 3, pp. 41–48, May/Jun. 2003.
- [13] C. F. Poets, "Pulse oximetry vs. transcutaneous monitoring in neonates: Practical aspects," Neonatology, Radiometer Medical A/S, Copenhagen, Denmark, 2003. [Online]. Available: www.bloodgas.com
- [14] W. van Weteringen et al., "Novel transcutaneous sensor combining optical tcPO₂ and electrochemical tcPCO₂ monitoring with reflectance pulse oximetry," *Med. Biol. Eng. Comput.*, vol. 58, no. 2, pp. 239–247, Feb. 2020.
- [15] A. Madan, "Correlation between the levels of SpO₂ and PaO₂," Lung India, vol. 34, pp. 307–308, 2017.
- [16] D. C. Hutchison et al., "Estimation of arterial oxygen tension in adult subjects using a transcutaneous electrode," *Thorax*, vol. 36, no. 6, pp. 473–477, Jun. 1981.
- [17] I. Costanzo et al., "An integrated readout circuit for a transcutaneous oxygen sensing wearable device," in *Proc. IEEE Custom Integr. Circuits Conf.*, 2020, pp. 1–4.
- [18] J. D. Tobias, "Transcutaneous carbon dioxide monitoring in infants and children," *Pediatr. Anesth.*, vol. 19, no. 5, pp. 434–444, 2009.
- [19] S. E. Huttmann et al., "Techniques for the measurement and monitoring of carbon dioxide in the blood," Ann. Amer. Thoracic Soc., vol. 11, no. 4, pp. 645–652, 2014.
- [20] I. Costanzo, D. Sen, J. Adegite, P. M. Rao, and U. Guler, "A noninvasive miniaturized transcutaneous oxygen monitor," *IEEE Trans. Biomed. Circuits Syst.*, vol. 15, no. 3, pp. 474–485, Jun. 2021.
- [21] I. Costanzo, D. Sen, and U. Guler, "A prototype towards a transcutaneous oxygen sensing wearable," in *Proc. IEEE Biomed. Circuits Syst. Conf.*, 2019, pp. 1–4.
- [22] I. Costanzo, D. Sen, J. McNeill, and U. Guler, "A nonuniform sampling lifetime estimation technique for luminescent oxygen measurements," in Proc. IEEE 48th Eur. Solid State Circuits Conf., 2022, pp. 413–416.
- [23] I. Costanzo, D. Sen, B. Giri, N. Pratt, P. Rao, and U. Guler, "Fluorescent intensity and lifetime measurement of platinum-porphyrin film for determining the sensitivity of transcutaneous oxygen sensor," in *Proc. IEEE Int. Symp. Circuits Syst.*, 2020, pp. 1–5.
- [24] J. P. Cascales et al., "Wearable device for remote monitoring of transcutaneous tissue oxygenation," *Biomed. Opt. Exp.*, vol. 11, no. 12, pp. 6989–7002, 2020.
- [25] S. Sonmezoglu et al., "Monitoring deep-tissue oxygenation with a millimeter-scale ultrasonic implant," *Nature Biotechnol.*, vol. 39, no. 7, pp. 855–864, 2021.
- [26] Y.-J. Choi and K. Sawada, "Physical sensors: Fluorescence sensors," in *Encyclopedia of Sensors and Biosensors*, 1st ed., Amsterdam, The Netherlands: Elsevier, 2022, pp. 1–19.
- [27] C. Albrecht, "Principles of fluorescence spectroscopy," Anal. Bioanalytical Chem., vol. 390, no. 5, pp. 1223–1224, Mar. 2008. [Online]. Available: https://doi.org/10.1007/s00216-007-1822-x
- [28] M. Y. Berezin and S. Achilefu, "Fluorescence lifetime measurements and biological imaging," Chem. Rev., vol. 110, no. 5, May 2010, Art. no. 2641.
- [29] E36103 Keysight A DC power supply, 20V, 40W 2 A: Product datasheet, 2019. Accessed: Dec. 05, 2022. [Online]. Available: https://literature.cdn. keysight.com/litweb/pdf/5992-0914EN.pdf?id=2633187
- [30] "Energizer CR2032: Product datasheet," Accessed: Dec. 05, 2022. [On-line]. Available: https://data.energizer.com/pdfs/cr2032.pdf
- [31] "Ocean Optics Inc. RedEye oxygen sensor patches," 2019. Accessed: Sep. 29, 2019. [Online]. Available: https://oceanoptics.com/product/redeyeoxygen-sensing-patches/
- [32] B. Kahraman et al., "Power and accuracy optimization for luminescent transcutaneous oxygen measurements," in *Proc. IEEE Int. Symp. Circuits Syst.*, 2022, pp. 1615–1619.
- [33] B. Kahraman et al., "A miniaturized prototype for continuous noninvasive transcutaneous oxygen monitoring," in *Proc. IEEE Biomed. Circuits Syst.* Conf., 2022, pp. 486–490.

- [34] "Analog devices inc. ADPD4101: Product datasheet and information," Accessed: Dec. 05, 2022. [Online]. Available: https://www.analog.com/en/products/adpd4101.html
- [35] "STMicroelectronics STM32WB35/55xx microcontroller: Product datasheet," Accessed: Dec. 05, 2022. [Online]. Available: https://www.st.com/resource/en/datasheet/stm32wb55cc.pdf
- [36] "STMicroelectronics STM32WB microcontrollers: Ultra-low-power features overview," Accessed: Dec. 05, 2022. [Online]. Available: https: //www.st.com/resource/en/application_note/an5071-stm32wb-seriesmicrocontrollers-ultralowpower-features-overview-stmicroelectronics. pdf
- pdf
 [37] "STMicroelectronics STM32WB35/55xx microcontroller: Reference manual," Accessed: Dec. 05, 2022. [Online]. Available: https://www.st.com/content/ccc/resource/technical/document/reference_manual/group0/83/cf/94/7a/35/a9/43/58/DM00318631/files/DM00318631.pdf/jcr:content/translations/en.DM00318631.pdf
- [38] "MATLAB fitnlm function: Fitting nonlinear regression model," Accessed: Jan. 18, 2023. [Online]. Available: https://www.mathworks.com/help/stats/fitnlm.html
- [39] G. A. Seber and C. J. Wild, Nonlinear Regression. Hoboken, NJ, USA: Wiley, 2003.
- [40] "CITI program research, ethics, compliance, and safety training," Accessed: Dec. 06, 2022. [Online]. Available: https://about.citiprogram.org/
- [41] "World Medical Association declaration of Helsinki: Ethical principles for medical research involving human subjects," Accessed: Dec. 06, 2022. [Online]. Available: https://www.wma.net/policies-post/wmadeclaration-of-helsinki-ethical-principles-for-medical-researchinvolving-human-subjects/
- [42] "The national map Advanced viewer," Accessed: Dec. 12, 2022. [Online]. Available: https://apps.nationalmap.gov/viewer/
- [43] "Air pressure at altitude calculator," Accessed: Dec. 12, 2022. [Online]. Available: https://www.mide.com/air-pressure-at-altitude-calculator
- [44] "Altitude to oxygen chart," Accessed: Dec. 12, 2022. [Online]. Available: https://milehightraining.com/altitude-to-oxygen-chart/
- [45] V. Valbuena et al., "Racial and ethnic bias in pulse oximetry and clinical outcomes," JAMA Intern. Med., vol. 182, no. 7, pp. 699–700, 2022.
- [46] Hypoxico sierra 100 altitude generator: Product information, Accessed: Dec.05, 2022. [Online]. Available: https://hypoxico.com/products/sierra-100.
- [47] S. Song et al., "A 769 uW battery-powered single-chip SoC with BLE for multi-modal vital sign monitoring health patches," *IEEE Trans Biomed Circuits Syst*, vol. 13, no. 6, pp. 1506–1517, Dec. 2019.
- [48] C.-J. Lim et al., "Wearable, luminescent oxygen sensor for transcutaneous oxygen monitoring," ACS Appl. Mater. Interfaces, vol. 10, no. 48, pp. 41026–41034, Jul. 2018.



Vladimir Vakhter (Graduate Student Member, IEEE) received degree Specialist (equivalent to B.S./M.S.) degree (with Hons.) in whectronics and automation of physical machines from the Ural Federal University (UrFU), Yekaterinburg, Russia, in 2016 and M.S. degree in electrical and computer engineering in 2021 from Worcester Polytechnic Institute (WPI), Worcester, MA, USA, where he is currently working toward the Ph.D. degree in ECE. He was the recipient of the Fulbright Grant He has more than 5 years of Professional Experience includes working

as an Electronics Engineer and Software Developer. For two and a half years, he conducted research on luminescent and scintillation materials with UrFU. Thereafter for two years, he developed a special magneto-optical system for the analysis of ferromagnets with the Russian Academy of Sciences. He completed two short-term scientific internships in the Superconducting Quantum Circuits Group with the Karlsruhe Institute of Technology (KIT), Karlsruhe, Germany in 2014 and 2015, respectively. His M.S. research with Integrated Circuits and Systems (ICAS) Laboratory, WPI was focused on the hardware security of next-generation biomedical devices, such as injectables, implantables, ingestibles, and wearables. His research interests include the ICAS Lab has been focused on Internet of Things (IoT) devices for medical applications, such as a compact pressure ulcer prevention system and a portable transcutaneous blood oxygen monitor, involving mixed-signal integrated circuit design, software development (including embedded), and printed circuit board (PCB) design.



Burak Kahraman (Graduate Student Member, IEEE) received the B.S. degree in electrical and electronics engineering from Middle East Technical University, Ankara, Turkey, in 2021. He is currently working toward the Ph.D. degree in electrical and computer engineering with Integrated Circuits and Systems (ICAS) Laboratory, Worcester Polytechnic Institute (WPI), Worcester, MA, USA. He completed two short-term summer internships at Scientific and Technological Research Council of Turkey (TUBITAK) and Military Electronics Indus-

try (ASELSAN) in 2019 and 2020, respectively. Thereafter for 8 months, he was a Candidate Engineer with ASELSAN with a focus on RF design. His research interests include the development of circuits and systems for biomedical sensors, with a focus on low-power analog/mixed-signal integrated circuits (ICs), and the Ph.D. research focuses on the development of wearable wireless sensors for the remote monitoring of transcutaneous blood gases. He is also a Reviewer for the IEEE conference ISCAS and the IEEE Transactions on Biomedical Circuits and Systems. He was the recipient of the Student Travel Grants from IEEE conferences including ISCAS and CICC in 2022.



Guixue Bu received the B.Eng. degree in biomedical engineering from Tsinghua University, Beijing, China, in 1993, and the M.S. and Ph.D. degrees in biomedical engineering from Purdue University, West Lafayette, IN, USA, in 2004 and 2008, respectively. He has a background in multimodality biomedical imaging, medical devices, biomedical signal measurement and processing, and cardiac electrophysicology. He had been an Imaging Scientist for 10 years before joining Analog Devices, Inc. in 2018, where he is currently a Systems Design Engineer

in the Instrumentation System Solutions Group. His research and development interests include vital signs monitoring technologies and systems, scientific instrumentation development and applications, and signal processing and algorithms.



Foroohar Foroozan (Senior Member, IEEE) received the Ph.D. degree in computer science and engineering from York University, Toronto, ON, Canada, in 2011. Since 2015, she has been with Digital Healthcare Business Unit with Analog Devices Inc. She is currently a Senior Manager of research science engineering, supervising a team of signal processing and machine learning engineers focused on developing algorithms (both embedded and cloud) for remote patient monitoring systems. From 2012 to 2013, she was a Postdoctoral Fellow with Sunnybrook research

institute working on 3D super-resolution ultrasound imaging for brain vascular mapping. From 2011 to 2013, she was also a Postdoc and a Lecturer with the Institute of Technology, University of Ontario, teaching Graduate (array processing and adaptive filtering) and Undergraduate (signal processing) courses. She is also a licensed Professional Engineer in Ontario, Canada.



Ulkuhan Guler (Senior Member, IEEE) received the B.Sc. degree in electronics and telecommunication engineering from Istanbul Technical University, Istanbul, Turkey, the M.E. degree in electronics engineering from the University of Tokyo, Tokyo, Japan, and the Ph.D. degree from Bogazici University, Istanbul, Turkey. She is currently an Assistant Professor of electrical and computer engineering with Worcester Polytechnic Institute (WPI), MA, USA. She was a Postdoctoral Researcher with Georgia Tech, GA, USA. Dr. Guler has co-authored three book chapters.

Her research interests include the broad area of circuits and systems, and her primary area of interest is analog/mixed-signal integrated circuits, circuit design of sensing interfaces, energy harvesting, wireless power transmission systems, and security for applications in healthcare. She was the recipient of the 2022 NSF CAREER Award. She is a TPC member of the IEEE CICC and IEEE BioCAS conferences. She is also serves as an Associate Editor for several journals, including IEEE SOLID-STATE CIRCUITS LETTERS (SSC-L), IEEE TRANSACTIONS ON BIOMEDICAL CIRCUITS AND SYSTEMS, and IEEE TRANSACTIONS ON CIRCUITS AND SYSTEMS II: EXPRESS BRIEFS. In addition, she is a member of several solid-state circuits and circuits and system communities, including the Women in Circuits Committee.